Elsevier Editorial System(tm) for Nuclear Engineering and Design
Manuscript Draft

Manuscript Number: NED-D-11-00083R1

Title: Extending Image Processing Strain Measurement System to Evaluate Fracture Behavior of Wall-Thinned Pipes

Article Type: Full Length Article

Corresponding Author: Mr. Masataka Tsuji,

Corresponding Author's Institution:

First Author: Masataka Tsuji

Order of Authors: Masataka Tsuji; Toshiyuki Meshii

Abstract: In this paper, an image processing strain measurement system was extended so that fracture behavior of wall-thinned pipes, such as out of plane and large plastic deformation observed in bulging, can be evaluated by the system. Regular grids with nominal size of 10 x 10 mm were marked on 100A carbon steel pipes and the images taken with 6 CCD cameras of 15 million pixels were correlated to achieve resolution of 0.3% strain. Strain of the cylinder outer surface was evaluated by 1) modeling the grids as a cylindrical shell, 2) measuring deformation of the grid on a projected plane, and 3) applying an updated Lagrangian method. The results indicate the possibility that the method is effective for the measuring large strains of wall thinned pipes observed before failure.

***Highlights**

> An image processing strain measurement system was proposed.

> The system can measure 1) out-of-plane deformation and 2) large strain.

> System was applied to wall thinned pipe (WTP) burst test, which bulging is observed.

> System was effective for understanding the unexpected burst location in a WTP.

*Title Page

Extending Image Processing Strain Measurement System to Evaluate Fracture Behavior of Wall-Thinned Pipes

Masataka TSUJI [a]*, Toshiyuki MESHII [b]

[a] Graduate Student, University of Fukui, 3-9-1 Bunkyo, Fukui, Fukui, JAPAN.

[b] Graduate School of Engineering, University of Fukui, 3-9-1 Bunkyo, Fukui, Fukui, JAPAN.

*Correspondent, E-mail: tsuji-m@u-fukui.ac.jp, FAX : +81-776-27-9764

Abstract

In this paper, an image processing strain measurement system was extended so that fracture behavior of wall-thinned pipes, such as out of plane and large plastic deformation observed in bulging, can be evaluated by the system. Regular grids with nominal size of 10 x 10 mm were marked on 100A carbon steel pipes and the images taken with 6 CCD cameras of 15 million pixels were correlated to achieve resolution of 0.3% strain. Strain of the cylinder's outer surface was evaluated by 1) modeling the grids as a cylindrical shell, 2) measuring deformation of the grid on a projected plane, and 3) applying an updated Lagrangian method. The validity of the system was confirmed by applying the proposed system to the burst tests of a wall-thinned cylinder. In addition the system measured the non-uniform strain distribution that explained the unexpected cracking location.

Key words: wall-thinned pipes, 3D movement analysis, image processing strain measurement system.

1. Introduction

The safety of wall-thinned pipes is primarily accomplished by the management of wall thickness, though researches on the structural integrity of the wall-thinned pipes is still being conducted in many countries (Bony et al., 2010; Chattopadhyay et al., 2009; Chiodo and Ruggieri, 2009; Hasegawa et al., 2008; Kim J-W et al., 2008; Kim Y-J et al., 2008; Na et al., 2006; Oh et al., 2009; Park et al., 2008; Takahashi et al., 2007; Zhu and Leis, 2007). Identification of the wall-thinning mechanism (Uchida et al., 2008) and an investigation of methods to evaluate the safety of wall-thinned pipes based on the correlation between flaw configuration and the fracture mode in the pipes (Hasegawa et al., 2011; Herman et al., 2009) is being conducted through the Research Project on Technical Information Basis for Aging Management (MRI, 2008), that is focused on nuclear power plants in Japan. The fracture position tended to differ from the position predicted from the designed thickness of the specimen in the many burst pressure tests in this project for pipes with relatively localized artificial wall-thinning (Hasegawa et al., 2011). This may be due to slight deviations in the machined wall thickness. If this happens for a test specimen, similar phenomenon will happen for in-service pipes. Because there is a need to reduce the over-conservatism in the existing methods, we thought that more elaborate fracture criteria were necessary. We also thought that the first step in accomplishing this objective was to realize strain distribution measurement over a relatively large area, in addition to where maximum strain is predicted. Another motivation was to

measure the strain until just before fracture, which exceeds the measurement limitations of the traditional strain gauges.

Therefore, in this research we measured the displacement of the outer surface of a cylinder using the image correlation method (Rastogi and Inaudi, 2000) and conducted strain distribution analysis for the lattice marked on the surface as finite elements (lattice method). Because the wall-thinned pipe tends to experience large strain and large deformation out of the plane of the lattice (bulging) just before the fracture, we enhanced the method so that it could be applied to burst pressure tests of locally wall-thinned pipes. In concrete, we evaluated the strain of the cylinder's outer surface by 1) modeling the grids as a cylindrical shell, 2) measuring deformation of the grid on a projected plane, and 3) applying an updated Lagrangian method.

2. Method to analyze the distribution of large-scale strain from an image of burst pressure test cylinders

The image correlation method has been applied over a very wide range in scale, from microscopic to gigantic, to measure displacement in two or three dimensions. One example in the microscopic range is the measurement of strain near a loaded crack tip using a scanning electron microscope (Johno et al., 1990), and an example in the gigantic range is the measurement of the movement of glaciers using speckle patterns from sunlight (Smith and North, 1999). There have been reports of the application of the image correlation method to measure displacement in cylinders

(Matsuda et al., 2008; Sakai et al., 2001), which is similar to our application. However, the first case focused on 3D displacement measurement under buckling (Matsuda et al., 2008), and the second case was a strain measurement for an in-plane lattice deformation (Sakai et al., 2001). Because a wall-thinned pipe tends to experience large strain and large deformation out of the plane of the lattice (bulging) just before the fracture, we made an enhancement to the image correlation method (lattice method) so that it could be applied to burst pressure tests of locally wall-thinned pipes. In the following, we discuss the displacement measurement system for the surface of a cylinder that we established using the image correlation method (lattice method), and then show the modifications required to actually measure large strain distribution in wall-thinned pipes.

2.1 System to analyze displacement on the outer surface of a cylinder

We prepared a 100x100x100 mm calibrator (Fig. 1 left) because this work was focused on a 100A wall-thinned pipe specimen. As we were drawing a lattice of approximately 10x10 mm on the surface of the pipe specimen (for every 10 degrees of angular coordinate and every 10 mm in the axial direction to be precise; Fig. 2), we prepared a single-lens reflex camera with 4752×3168 (about 15 million) pixels to achieve a resolution of approximately 0.2% strain per pixel when the calibrator covered the entire space of the photo taken. The result of our selection was nominal strain resolution of (100mm/3168) /10 mm x100 % = 0.3%, by correlating 100 mm of the calibrator with 3168 pixels, and correlating the minimum unit of deformation of the 10 mm grid to a single pixel.

Six cameras were placed at regular intervals around the specimen to observe the deformation behavior of the entire surface of the specimen (Fig. 3, photo) because it is necessary to use more than two cameras to track every lattice point with the three-dimensional motion analysis software mentioned below. We decided the number of cameras as six, by considering that the area of the pipe which one camera can capture was approximately 120 deg.

These six cameras were used to take images of the calibrator before the experiment, that is, to build a coordinate system in virtual space with three-dimensional motion analysis software (DITECT, 2011) from the images based on the method of direct linear transformation (DLT) (Hartley and Zisserman, 2003).

2.2 Enhancement in the method to analyze large strains on the outer surface of the cylinder

The pipe specimen in this work is a wall-thinned cylinder with an inner radius to wall thickness ratio of about 12, so it is viewed as a cylindrical shell. If the deformation of the lattice can be taken as in-plane or, in other words, if we can assume that the lattice remains parallel to the cylinder axis before and after the deformation, then 2D displacement information is enough for strain analysis as reported previously (Sakai et al., 2001). However, to handle cases in which the lattice after deformation does not remain parallel to the cylinder axis (out-of-plane deformation) such as bulging, we thought that the following steps were necessary: 1) all the three dimensional displacement components should be measured, and then 2) a projection of the lattice on the surface of the cylinder

should be made before (time step i) and after (time step i+1) deformation on the identical plane, allowing 3) consideration of the change in shape of the lattice and evaluation of the strain increment of the lattice with the updated Lagrangian approach.

In other words, we look at an element composed of lattice points 1 to 4 drawn on the surface of the specimen cylinder at time step i, and consider the local coordinate system (X, Y, Z) which has point 1 as the origin (Fig. 4).

$$\begin{Bmatrix} \mathrm{X} \\ \mathrm{Y} \\ \mathrm{Z} \end{Bmatrix} = \Lambda \begin{Bmatrix} x - x_1 \\ y - y_1 \\ z - z_1 \end{Bmatrix} \tag{1}$$

Here, (X_j, Y_j, Z_j) (j = 1~4) is the coordinate of the lattice points on the original (x, y, z) coordinate system, and Λ is the directional cosine matrix.

$$\Lambda = \begin{bmatrix} \cos(\mathrm{X},x) & \cos(\mathrm{X},y) & \cos(\mathrm{X},z) \\ \cos(\mathrm{Y},x) & \cos(\mathrm{Y},y) & \cos(\mathrm{Y},z) \\ \cos(\mathrm{Z},x) & \cos(\mathrm{Z},y) & \cos(\mathrm{Z},z) \end{bmatrix} = \begin{bmatrix} \Lambda_{\mathrm{X}x} & \Lambda_{\mathrm{X}y} & \Lambda_{\mathrm{X}z} \\ \Lambda_{\mathrm{Y}x} & \Lambda_{\mathrm{Y}y} & \Lambda_{\mathrm{Y}z} \\ \Lambda_{\mathrm{Z}x} & \Lambda_{\mathrm{Z}y} & \Lambda_{\mathrm{Z}z} \end{bmatrix} \tag{2}$$

Choosing the Z-axis perpendicular to the rectangle element 1234, elements of Λ may be defined as follows. The rectangle 1234 is divided into triangles 124 and 234, and the local coordinate system (X, Y, Z) is selected such that the triangle 124 and the Z-axis are perpendicular to each other. Here, the origin of the local coordinate system is taken at point 1, and the X-axis is taken along edge 1-2. The vector $\mathbf{v}_{21}$ defining this edge 1-2 becomes

$$\mathrm{v}_{21} = \begin{Bmatrix} x_2 - x_1 \\ y_2 - y_1 \\ z_2 - z_1 \end{Bmatrix} = \begin{Bmatrix} x_{21} \\ y_{21} \\ z_{21} \end{Bmatrix} \tag{3}$$

Here, the directional cosine in the X direction $\mathbf{v}_{\mathrm{X}}$ is

$$\mathrm{v_X} = \begin{Bmatrix} \Lambda_{Xx} \\ \Lambda_{Xy} \\ \Lambda_{Xz} \end{Bmatrix} = \frac{1}{l_{21}} \begin{Bmatrix} x_{21} \\ y_{21} \\ z_{21} \end{Bmatrix} \quad l_{21} = \sqrt{x_{21}^2 + y_{21}^2 + z_{21}^2} \tag{4}$$

As the Z-axis must be perpendicular also to edge 1-4, by defining the edge 1-4 as $\mathbf{v}_{41}$

$$\mathrm{v}_{41} = \begin{Bmatrix} x_4 - x_1 \\ y_4 - y_1 \\ z_4 - z_1 \end{Bmatrix} = \begin{Bmatrix} x_{41} \\ y_{41} \\ z_{41} \end{Bmatrix} \tag{5}$$

and noticing that the cross product of $\mathbf{v}_{21}$ and $\mathbf{v}_{41}$

$$\mathrm{v}_{21} \times \mathrm{v}_{41} = \begin{Bmatrix} y_{21}z_{41} - z_{21}y_{41} \\ z_{21}x_{41} - x_{21}z_{41} \\ x_{21}y_{41} - y_{21}x_{41} \end{Bmatrix} = \begin{Bmatrix} yz_{124} \\ zx_{124} \\ xy_{124} \end{Bmatrix} \tag{6}$$

is perpendicular to both vectors, dividing by its length 2Δ yields the directional cosine $\mathrm{v_Z}$.

$$\mathrm{v_Z} = \begin{Bmatrix} \Lambda_{Zx} \\ \Lambda_{Zy} \\ \Lambda_{Zz} \end{Bmatrix} = \frac{1}{2\Delta} \begin{Bmatrix} yz_{124} \\ zx_{124} \\ xy_{124} \end{Bmatrix} \tag{7}$$

$$2\Delta = \sqrt{(yz_{124})^2 + (zx_{124})^2 + (xy_{124})^2} \tag{8}$$

The directional cosine $\mathrm{v_Y}$ can be obtained similarly as

$$\mathrm{v_Y} = \Lambda_{\mathrm{Y}} = \mathrm{v_Z} \times \mathrm{v_X} \tag{9}$$

After the coordinates of the four nodes at time step *i* are determined with the above method, the corresponding lattice at time step *i*+1 is projected on this (X, Y) plane. Assuming this rectangle element deforms on this plane with time steps *i*→ *i*+1, the B-matrix of the element at time *i* is obtained from the displacement of nodes in *i*→*i*+1

$$\{\Delta U\}_{i\to i+1}=\begin{Bmatrix} X_{1,i+1}-X_{1,i} \\ Y_{1,i+1}-Y_{1,i} \\ \vdots \\ Y_{4,i+1}-Y_{4,i} \end{Bmatrix} \tag{10}$$

on the (X, Y) plane. The incremental strain of the lattice ($\Delta\varepsilon_X$, $\Delta\varepsilon_Y$, $\Delta\gamma_{XY}$) is obtained from this displacement, and the strain at any given time step is defined as the sum of incremental strain up to that time step.

$$\begin{Bmatrix} \Delta\varepsilon_X \\ \Delta\varepsilon_Y \\ \Delta\gamma_{XY} \end{Bmatrix}_{i\to i+1}=[B]_i\{\Delta U\}_{i\to i+1} \quad \therefore \begin{Bmatrix} \varepsilon_X \\ \varepsilon_Y \\ \gamma_{XY} \end{Bmatrix}_{i+1}=\sum_{j=1}^{i}\begin{Bmatrix} \Delta\varepsilon_X \\ \Delta\varepsilon_Y \\ \Delta\gamma_{XY} \end{Bmatrix}_{j\to j+1} \tag{11}$$

3. Experiment (example of application)

3.1 Specimen

The pipe specimen is made of carbon steel STPT370. Tensile test results of STPT370 are given in Table 1, and the chemical composition in Table 2. Figure 5 shows the configuration of the specimen. Here, ϕ is position of the circumferential direction of the pipes in which $\phi = 0$ and $z = 0$ specifies the center of the artificial flaw. Note that ϕ was measured in the clockwise direction. The outer diameter D_0＝107.1 mm, nominal wall thickness t＝4 mm, and the wall-thinned section was machined to a thickness t_1＝2 mm. The size of this artificial flaw was δ_z＝6 mm in the axial direction and θ＝23.3 deg in the circumferential direction. Figure 6 shows the measured wall thickness in the plane of $z = 0$ mm in Fig. 5 where a crack is predicted to initiate. Here, Fig. 6 (a) shows the thickness distribution of a non-flawed section and Fig. 6 (b) shows an artificial flawed section. In Fig. 6 (a), the maximum

thickness was 4.017 mm and the minimum was 3.964 mm, therefore the deviation from nominal thickness t = 2 mm was as small as +0.5~–1%. On the other hand, in Fig. 6 (b), the maximum thickness was 2.097 mm and the minimum was 2.092 mm, therefore the deviation in the wall-thinned section t_1 was as large as +5% from the design value, though the distribution appeared to be uniform. Similar wall thickness distributions were observed for other planes normal to the z-axis, predicting that a crack will form at the center of the groove.

3.2 Set up of the image-based strain measurement system

The concrete process of the camera setting is as follows. First, we put the specimen on the specimen holder shown in the photo in Fig. 3. Here, ξ, η and ζ are orthogonal coordinate systems of camera positions, and α is the tilt angle of the camera on the $\xi\eta$-plane at specifie ζ. In addition, (ξ, η) = (0, 0) is the axis center of the specimen and ζ = 0 represents the floor level.

The specimen was placed so that the circumferential center of the artificial flaw was near the ξ-axial forward direction, and cameras 1 and 2 were set at $\pm$30 deg intervals from the ξ-axis. Cameras 3-6 were set at 60 deg intervals. Then, the initial value of ζ was set as 350 mm to capture the center of the artificial flaw.

Location of the camera was determined by adjusting two parameters; that is, $R = (\xi^2+\eta^2)^{0.5}$: the distance from a camera to the specimen axis center and α. The concrete process is as follows.

Process to determine R The initial value was set as 600 mm, in order to keep the cameras very

close to the protective wall. It was done to prevent the water jet from falling on the cameras when the specimen bursts, and to make it easy to focus the cameras.

Process to determine α The initial value of α was set as 0 and values 15, 30, 45, and 60 deg were also tried. As a result, we chose α = 30 deg, considering the balance that large α is necessary to realize an accurate depth length in the images, but images deflected when α was too big. Then, the final value of ζ was obtained as 850 mm from the results in R and α above. Given the above-mentioned results, the determined position of cameras are in Table 3.

Next we exchanged the specimen with the calibrator (Fig. 1, left) as the final process of set up, to build a coordinate system in virtual space. First, we placed the calibrator so that it's center coincided with the center of the specimen, in concrete (ξ, η, ζ) = (0, 0, 350) in Fig. 3. Secondly, we turned the calibrator around without changing the position of the center of the calibrator so that a difference of the distance between the balls for nominal value 100 mm was less than 0.5% in 3-D virtual space. The final coordinates of the eight balls in 3-D virtual space are shown in Table 4. We see from Table 4 that the error is less than 0.5 mm, and small compared with the side length of 100 mm. Although the optimum setup will change with the specifications of the cameras used (such as focal length), the setup shown is a good base example.

3.3 Testing system and results

Figure 7 (a) is a schematic of the testing system, which is comprised of a pressure system

driven by a hydraulic pump, an analogue measurement system of pressure sensors and strain gauges, and a digital image measurement system with six high resolution single-reflex cameras (4752×3168 pixels or about 15 million pixels each).

After securing the specimen on the floor behind protective walls, various sensors were connected before starting a burst pressure test. The specimen was pressurized at an air flow rate of 1 ～6 *l*/min from the compressor. Defining the effective pressurization rate as the maximum internal pressure divided by the duration of pressurization, the effective pressurization rate for the specimen was below 0.4 MPa/min. The pressurization rate just before the burst was less than 0.1 MPa/min, and the internal pressure at the burst was p_f＝31.2 MPa (Fig. 8). We took pictures every 1 MPa until the internal pressure increased to 20 MPa, and after that we took pictures every five seconds.

3.4 Calibration of the image based strain measurement system with strain gauges

Strain obtained by the proposed image based system was compared with that measured by strain gauges, located at positions shown in Table 5 and Fig. 7(b). Results are summarized in Figs. 9~11 to confirm the validity of the proposed image-based strain measurement system. Here, the strain gauges were located at the centroids of the lattice, to directly compare the strain with that evaluated by the image-based method. We limited the number of strain gauges to six, because there was a possibility of strain gauges disturbing the image-based method by hiding lattice points. In concrete, we placed circumferential strain gauges ① and ② near the artificial flaw section; i.e. ①

at (ϕ, z) = (-5, 15) and ② at (ϕ, z) = (15, 15). We placed circumferential strain gauge ③ very far from the artificial flaw section at (ϕ, z) = (175, -5). We placed axial strain gauges ④~⑥ at positions symmetrical to gauges ①~③; in concrete, ④ at (ϕ, z) = (5, 15), ⑤ at (ϕ, z) = (15, -15) and ⑥ at (ϕ, z) = (-175, -5). Though we do not show specific results of the axial strain where the measured strain was less than the resolution, large discrepancies were observed, as expected. We focused on the circumferential strain, which is the maximum principle strain.

Regarding Figs. 9~11, we expected that the circumferential strain in Fig. 9 was the maximum, because strain gauge ① was the nearest to the artificial flaw. As was expected, such a result was obtained in both the strain gauge and the proposed method. In the range of p up to approximately 20 MPa, and when the pipe was in the elastic range, circumferential strain ε_θ evaluated by the proposed method showed a discrepancy with that measured by the strain gauges. This was not surprising, because the accuracy of the proposed method is 0.3% strain. However, after yielding, the measured ε_θ from the images matched well with the values measured with the strain gauges. In addition, although the internal pressure decreased for a while, after the pressure reached approximately 20 MPa, the strain increased in both the strain gauge and the proposed method. We see from Fig. 8 that the cause of the pressure decrement around 20 MPa was the start of plastic deformation; i.e., the rate of pressurization was less than the rate of deformation. Thus, the behavior in strain with the onset of plastic deformation could be observed in the proposed method. From these results, we conclude that

the measurement of strain from the images in this work is a valid methodology.

3.5 Strain distribution just before burst, fracture mode, and fracture position

Though the specimen in this work had a long groove in the circumferential direction (flaw aspect ratio $\delta_z/(\theta R_m)$=0.29), axial cracking was observed as shown in Fig. 12. This observation is supported by the occurrence of a long axial strain concentration seen in Fig. 13, which is the circumferential strain distribution obtained by our image based strain measurement system just before fracture. Furthermore, the measured strain distribution explains the trend for cracking to occur at a different position from that predicted based on the designed wall thickness.

We believe that the rationality of the strain measurement method using images as in this work has been justified. We expect this method will be utilized in measuring the strain distribution in pipe specimens, and in the future to explain the fracture mode and position of fracture.

4. Discussion

In this experiment, the location of the crack was not the center of the artificial flaw, but ϕ = 7 deg, z = 0~5 mm. Thus, there might be an opinion that the location of the point with the maximum circumferential strain in Fig. 13 is different from where the crack initiated, and thus “how can we predict failure of a pipe with the proposed method?” To examine this, we show in Fig. 14 the enlarged area of the artificial flaw from Fig. 13, and superimposed a lattice over it. The X mark in Fig. 14 is the centroids of the lattice, and the white circles represent the lattice points that were

drawn on the pipe. We calculated the circumferential strain of the X-marked positions with the proposed method, and we made a circumferential strain interpolation using graphic software from the evaluated results on the X points in Fig. 14. Considering that the cracking occured in the lattice ‘bghc’ and that the maximum value of circumferential strain occured at this lattice (in concrete, the centroid in this lattice), we believe our method gave a good estimate on the location of cracking.

There might be another opinion that strain measurement by the traditional strain gauge is more simple and practical compared to the proposed method. However, as shown is Fig. 13, distribution in the wide region can be measured by the proposed method, which is difficult with the strain gauge method. In addition, measuring large strains, such as in case of bulging, is possible by the proposed method. We consider these two merits of the proposed method to be worth making the set-up efforts.

5. Conclusion

We have described fracture behavior evaluation of wall-thinned pipes by an image processing strain measurement system. Regular grids with nominal size of 10 x 10 mm were marked on 100A carbon steel pipes, and images taken with 6 CCD cameras of 15 million pixels were correlated to achieve resolution of 0.3% strain. Strain of the cylinder’s outer surface was evaluated by 1) modeling the grids as a cylindrical shell, 2) measuring deformation of the grid on a projected plane, and 3) applying an updated Lagrangian method. The validity of the system was confirmed by applying the proposed system to the burst tests of a wall-thinned cylinder. In addition the system

measured the non-uniform strain distribution that explained the unexpected cracking location. We expect this method will be utilized in measuring the strain distribution of pipe specimens, and in the future to explain the fracture mode and position of fracture.

Acknowledgement

The experiment was done under the support of NISA project on Enhancement of Ageing Management and Maintenance of Nuclear Power Stations. Their support is greatly appreciated. The authors also thank the students and staff who participated in this project.

List of Tables

Table 1 Tensile test results

Material	Size	σ_{YS0} (MPa)	σ_{B0} (MPa)	ε_{B0}
JIS－STPT370	100A	255	416	0.45

Table 2 Chemical composition of the specimen

C	Si	Mn	P	S	Cu	Ni	Cr	Mo
0.15	0.19	0.48	0.018	0.006				

Table 3 Optimized installation position of cameras

camera	ξ (mm)	η (mm)	ζ (mm)	α (deg)
1	520	300	850	30
2	520	-300		
3	0	-600		
4	-520	-300		
5	-520	300		
6	0	600		

Table 4 Calibration result

point	measured (mm)			reference (mm)			error
	x	*y*	*z*	*x*	*y*	*z*	(distance, mm)
1	-0.17	100.27	0.22	0	100	0	0.39
2	-0.08	100.17	99.76	0	100	100	0.30
3	0	0	0	0	0	0	base
4	0.14	-0.34	100.03	0	0	100	0.37
5	100.34	99.70	-0.11	100	100	0	0.47
6	99.77	99.99	100.13	100	100	100	0.26
7	99.71	0.15	-0.12	100	0	0	0.35
8	100.06	0.307	100.08	100	0	100	0.32

Table 5 Location of strain gauges

	Circumferential			Axial		
	①	②	③	④	⑤	⑥
ϕ (deg)	-5	15	175	5	15	-175
z (mm)	15	15	-5	15	-15	-5

List of Figures

*Bibliography
Click here to view linked References

References

Bony, M., Alamilla, J. L., Vai, R., Flores, E. 2010. Failure Pressure in Corroded Pipelines Based on Equivalent Solutions for Undamaged Pipe. Journal of Pressure Vessel Technology-Transactions of the Asme. 132.

Chattopadhyay, J., Kushwaha, H. S., Roos, E. 2009. Improved integrity assessment equations of pipe bends. International Journal of Pressure Vessels and Piping. 86, 454-473.

Chiodo, M. S. G., Ruggieri, C. 2009. Failure assessments of corroded pipelines with axial defects using stress-based criteria: Numerical studies and verification analyses. International Journal of Pressure Vessels and Piping. 86, 164-176.

Hartley, R., Zisserman, A., 2003. Multiple View Geometry in computer vision. Cambridge University Press.

Hasegawa, K., Miyazaki, K., Nakamura, I. 2008. Failure mode and failure strengths for wall thinning straight pipes and elbows subjected to seismic loading. Journal of Pressure Vessel Technology-Transactions of the Asme. 130.

Hasegawa, K., Meshii, T., Scarth, D. A., 2011. Assessment of piping field failures and burst tests on carbon steel pipes with local wall thinning using ASME section XI code case N-597-2. Transactions of ASME, Journal of Pressure Vessel Technology. 133, 031101-1-10

Herman, I., Kuwazuru, O., Meshii, T., 2009. Effect of Flaw Geometry on the Fracture Behavior of Wall-thinned Pipe under Internal Pressure. Proceeding of 12 th International Conference on Fracture. Ottawa, Canada. 1-10.

Johno, M., Sugeta, J., Takarada, S., Ohkubo, H., Komajoh, M., 1990. Development of computer image processing technique and direct observation of fatigue crack growth behavior by field emission type scanning electron microscope (in Japanese). Journal of the Society of Materials Science, Japan. 39(446), 1583-1589.

Kim, J. W., Na, M. G., Park, C. Y., 2008. Effect of local wall thinning on the collapse behavior of pipe elbows subjected to a combined internal pressure and in-plane bending load. Nuclear Engineering and Design. 238, 1275-1285.

Kim, Y. J., Kim, J., Ahn, J., Hong, S. P., Park, C. Y., 2008. Effects of local wall thinning on plastic limit loads of elbows using geometrically linear FE limit analyses. Engineering Fracture Mechanics. 75, 2225-2245.

Matsuda, H., Cheng, C., Furuya, S., Uetuma, H., Yamashita, T., Huang, M., 2008. Visualization of buckling of thin-walled cylindrical shell by Digital image correlation method. Proceedings of JSEM. 12-17.

Na, M. G., Kim, J. W., Hwang, I. J., 2006. Estimation of collapse moment for the wall-thinned pipe bends using fuzzy model identification. Nuclear Engineering and Design. 236, 1335-1343.

Oh, C. K., Kim, Y. J.and Park, C. Y., 2009. Effects of local wall thinning on net-section limit loads for pipes under combined pressure and bending. Nuclear Engineering and Design. 239, 261-273.

Park, J. H., Shin, K. I., Park, C. Y., Lee, S. H., 2008. Allowable local thickness of wall-thinned straight pipes in ASME Code Case N-597-2. International Journal of Pressure Vessels and Piping. 85, 620-627.

Rastogi, P., Inaudi, D., 2000. Trends in Optical Non-Destructive Testing and Inspection. Elsevier Science.

Sakai, M., Matsuo, T., Onitsuka, S., Harada, M., 2001. Image measurement in the local transformation point of the cylinder type RC structure (in Japanese). Journal of Japan concrete institute. 23(3), 1141-1146.

Smith, E. W., North, H. C., 1999. Sunlight Illuminated Speckle Photography. ATEM9. 611-616.

Takahashi, K., Kato, A., Ando, K., Hisatsune, M., Hasegawa, K., 2007. Fracture and deformation behaviors of tee pipe with local wall thinning. Nuclear Engineering and Design. 237, 137-142.

Uchida, S., Naitoh, M., Uehara, Y., Okada, H., Hiranuma, N., Sugino, W., Koshizuka, S., 2008. Evaluation Methods for Corrosion Damage of Components in Cooling Systems of Nuclear Power Plants by Coupling Analysis of Corrosion and Flow Dynamics (II): Evaluation of Corrosive Conditions in PWR Secondary Cooling System. Journal of Nuclear Science and Technology. 45, 1275-1286.

Zhu, X. K., Brian, L., 2007. Theoretical and numerical predictions of burst pressure of pipelines. Journal of Pressure Vessel Technology-Transactions of the Asme. 129, 644-652.

Web References

MRI, 2008, <http://nisaplm.jp/>,. (accessed 2011-02-08).

DITECT, 2011, <http://www.ditect.co.jp/>, . (accessed 2011-02-08).

Figure

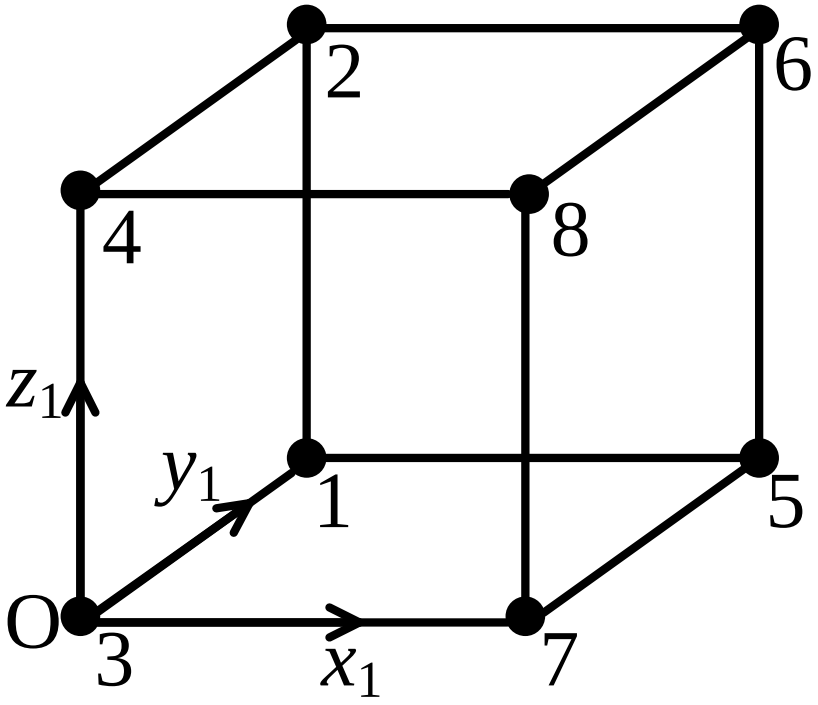

Fig. 1 Calibrator

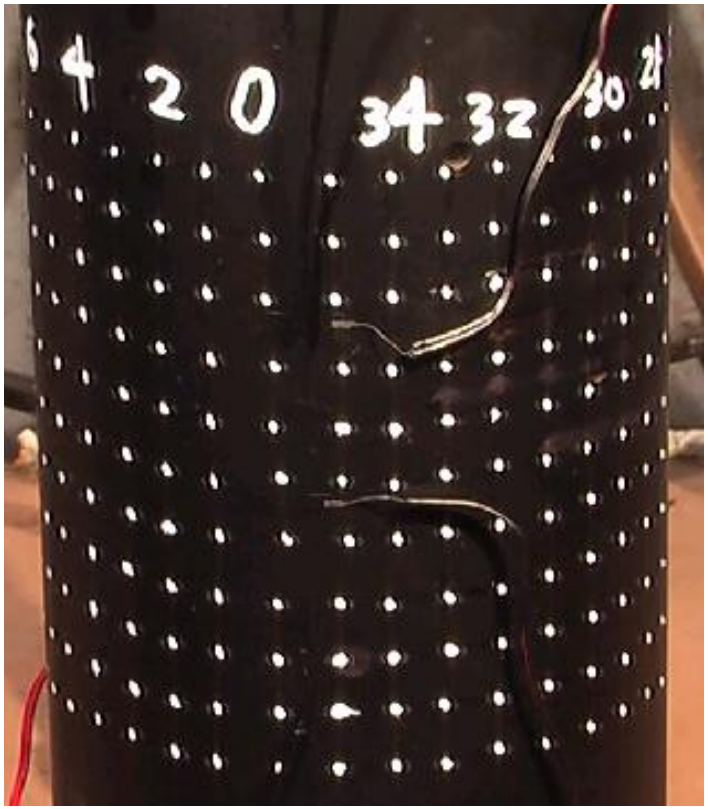

Fig. 2 Marked pipe

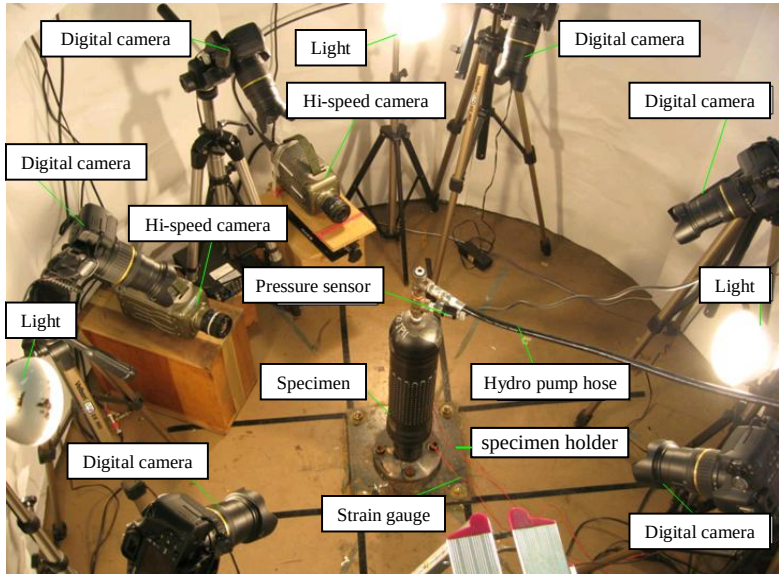

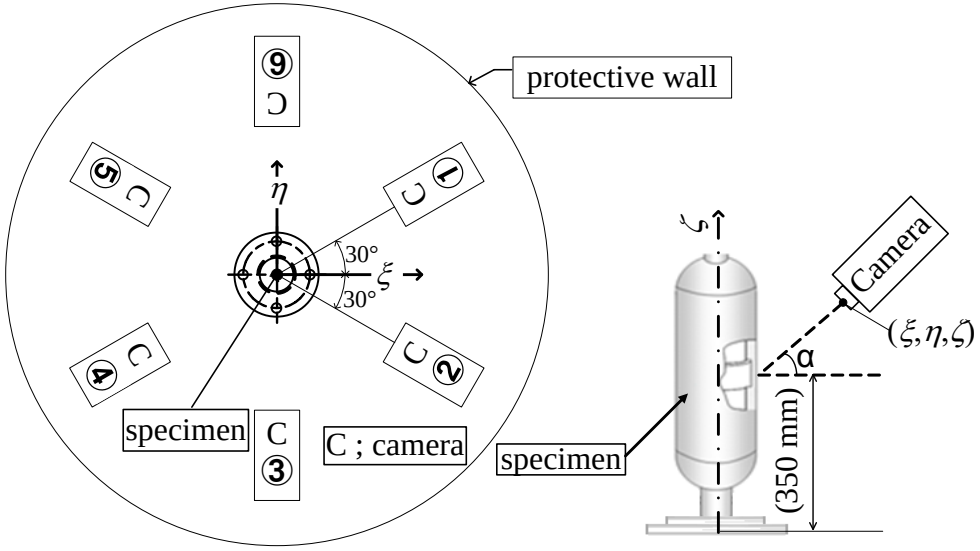

Fig. 3 Installation position of cameras

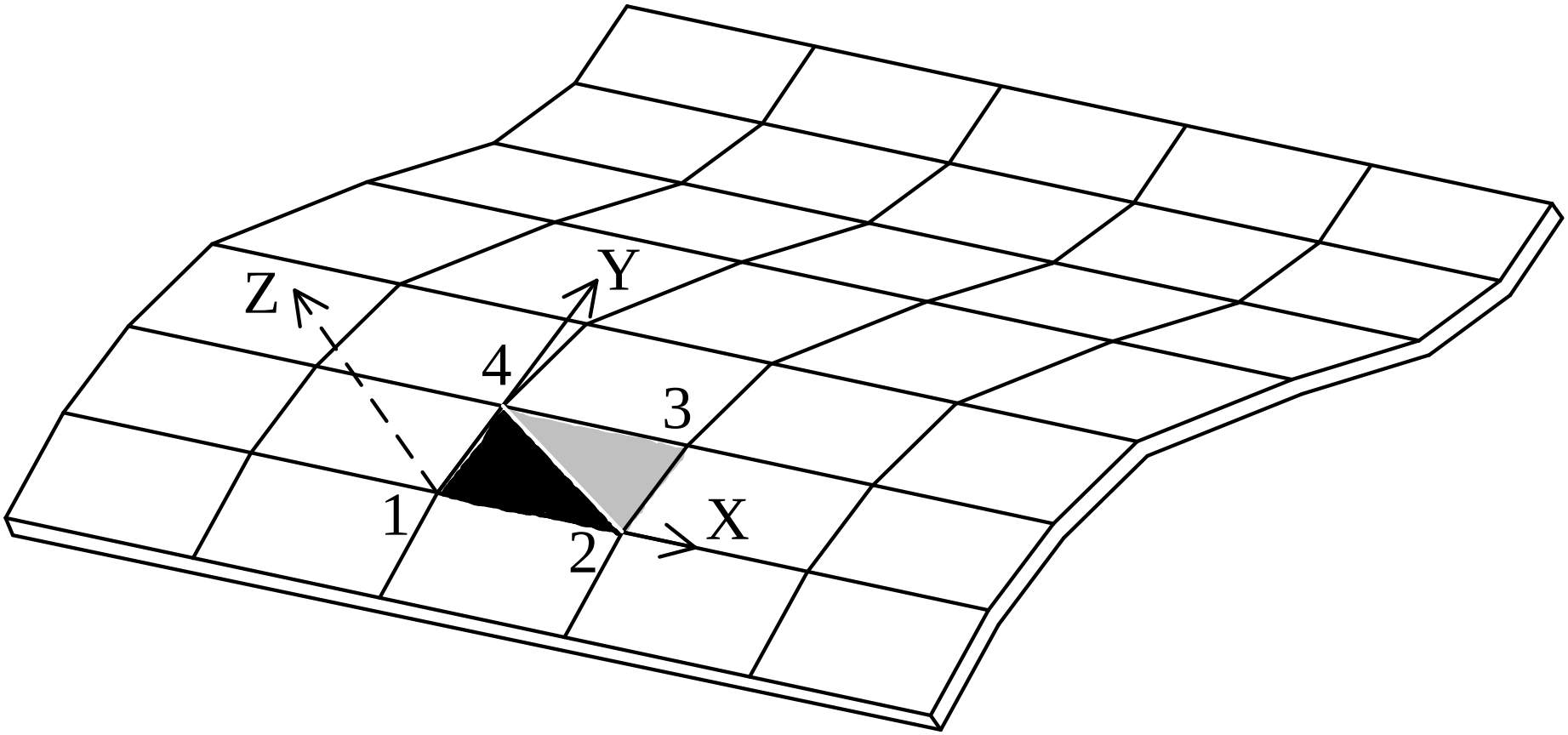

Fig. 4 Cylindrical shell model

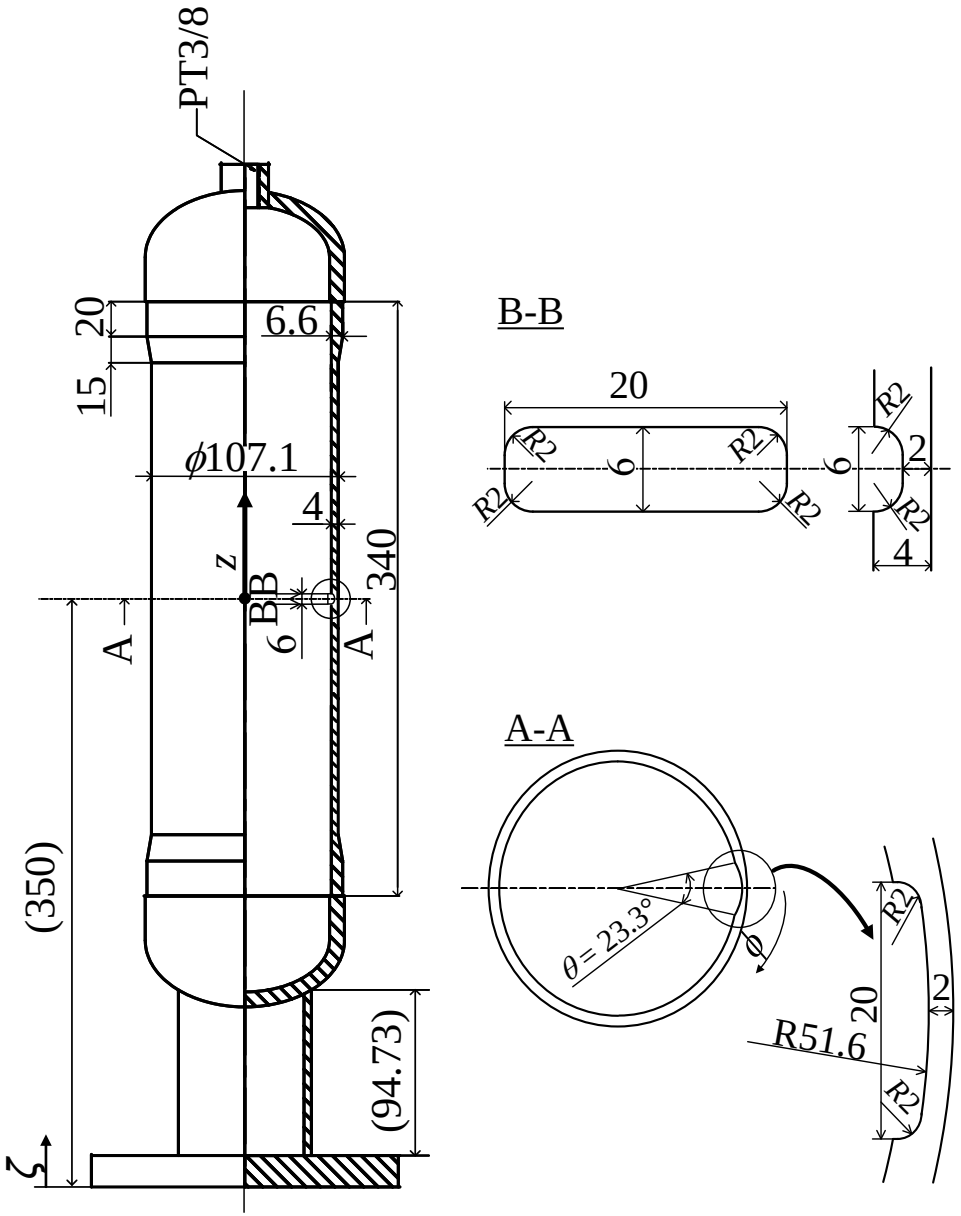

Fig. 5 Specimen configuration

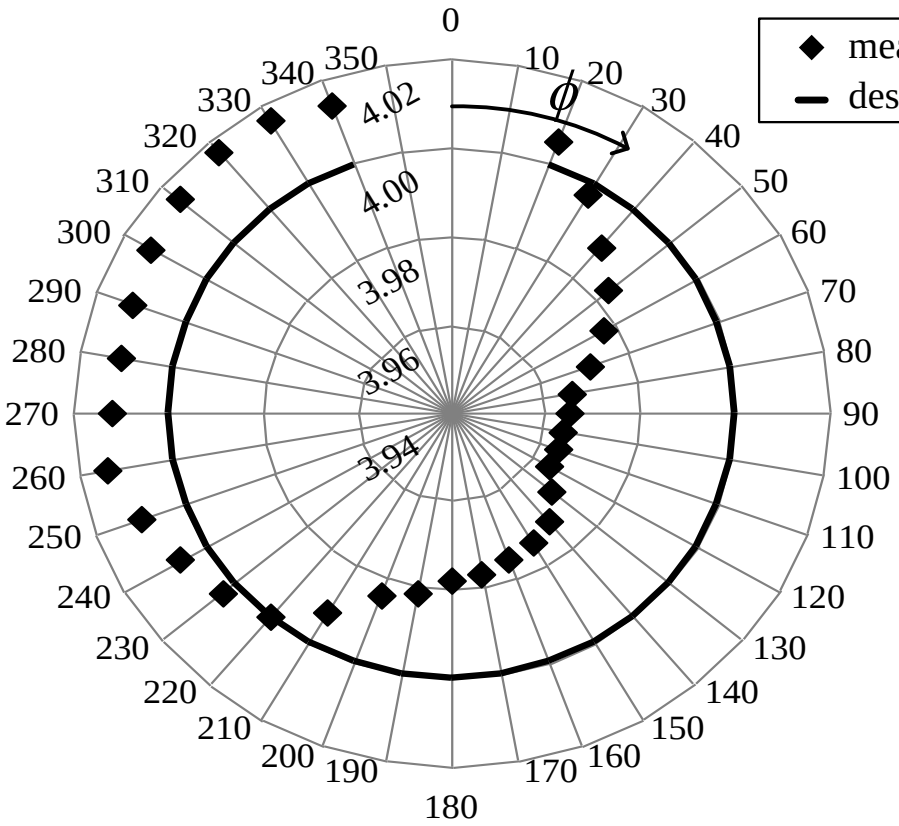

(a) non-flawed section

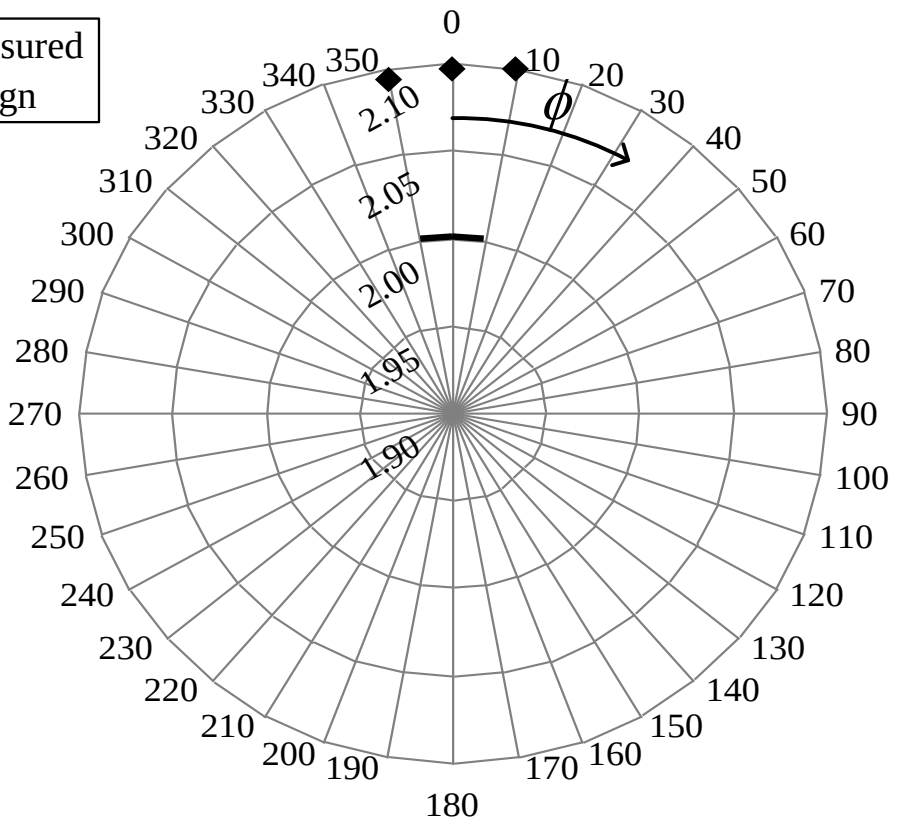

(b) artificial flawed section

Fig. 6 Design and measured wall thickness at z = 0 plane

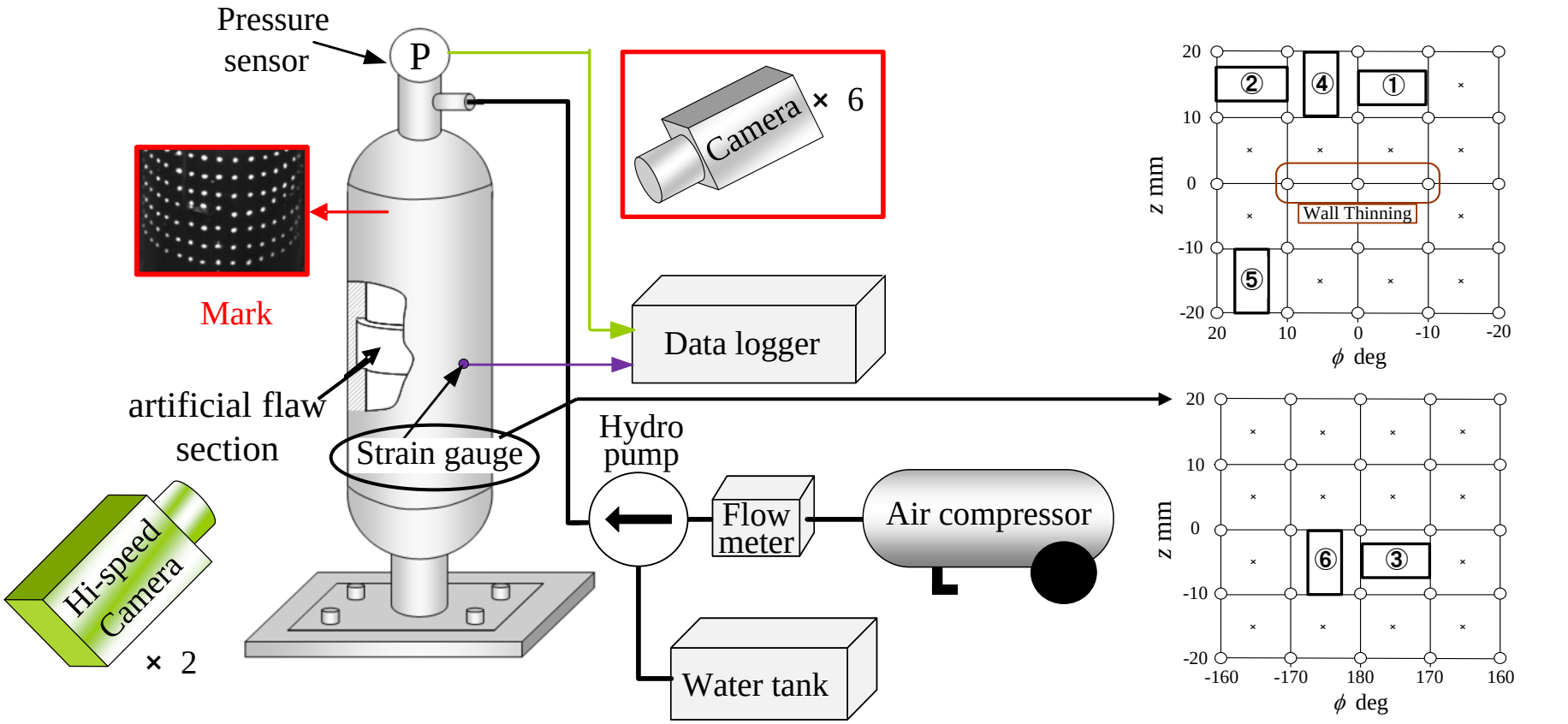

(a) Schematic of the system

(b) Location of strain gauges

Fig. 7 Testing system

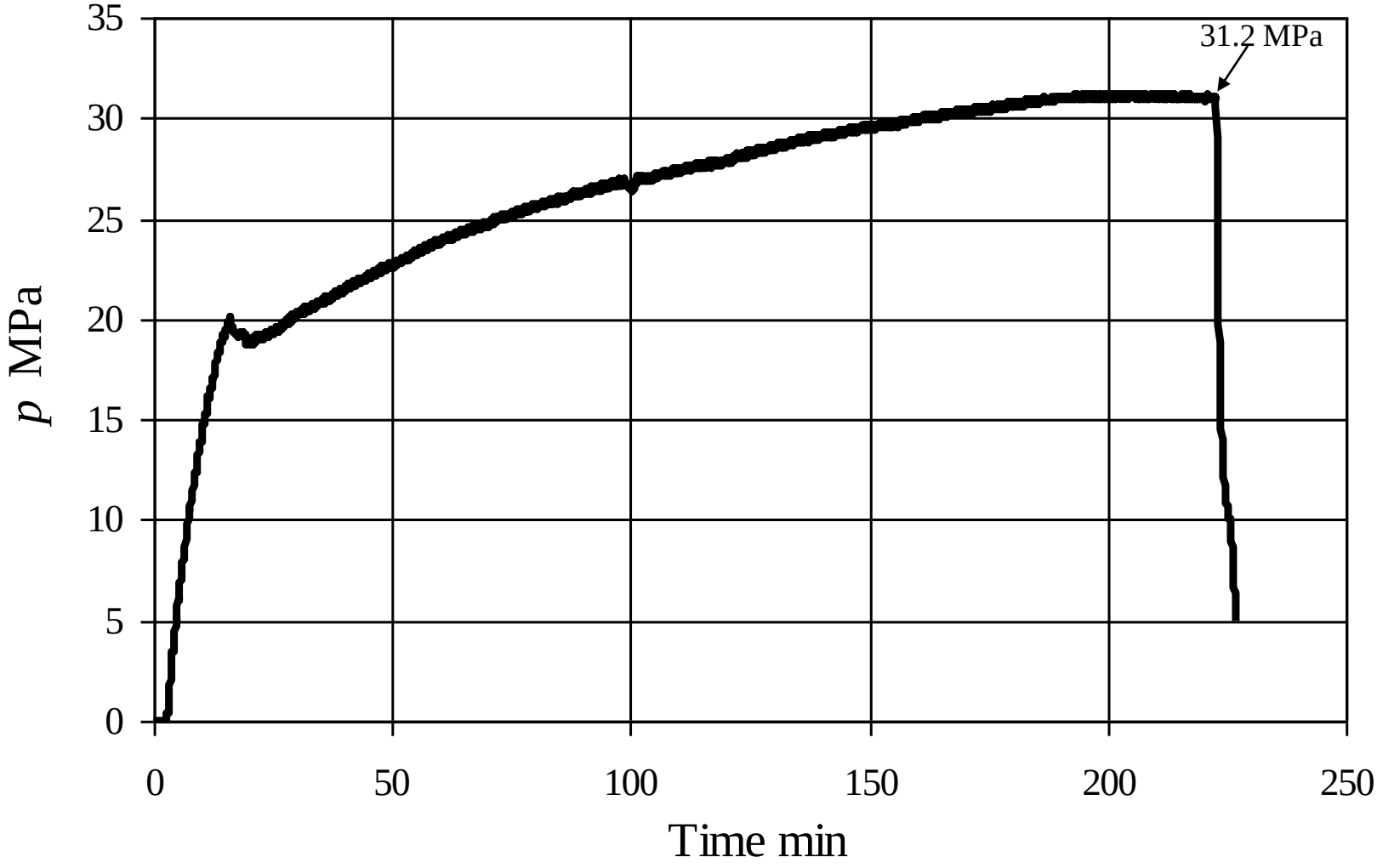

Fig. 8 Trends in test pressure

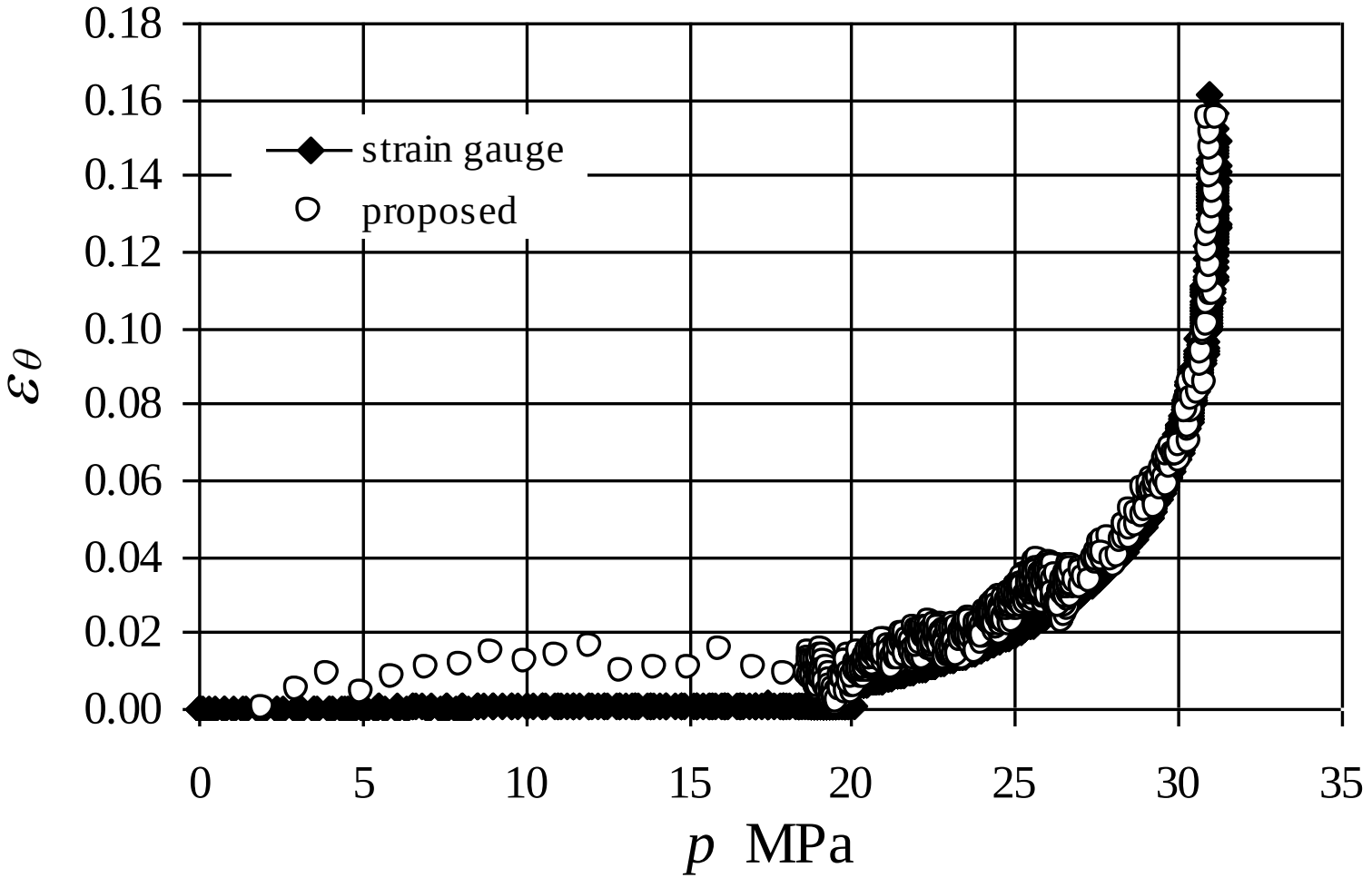

Fig. 9 Internal pressure-circumferential strain curve (ϕ = -5 deg, z = 15 mm)

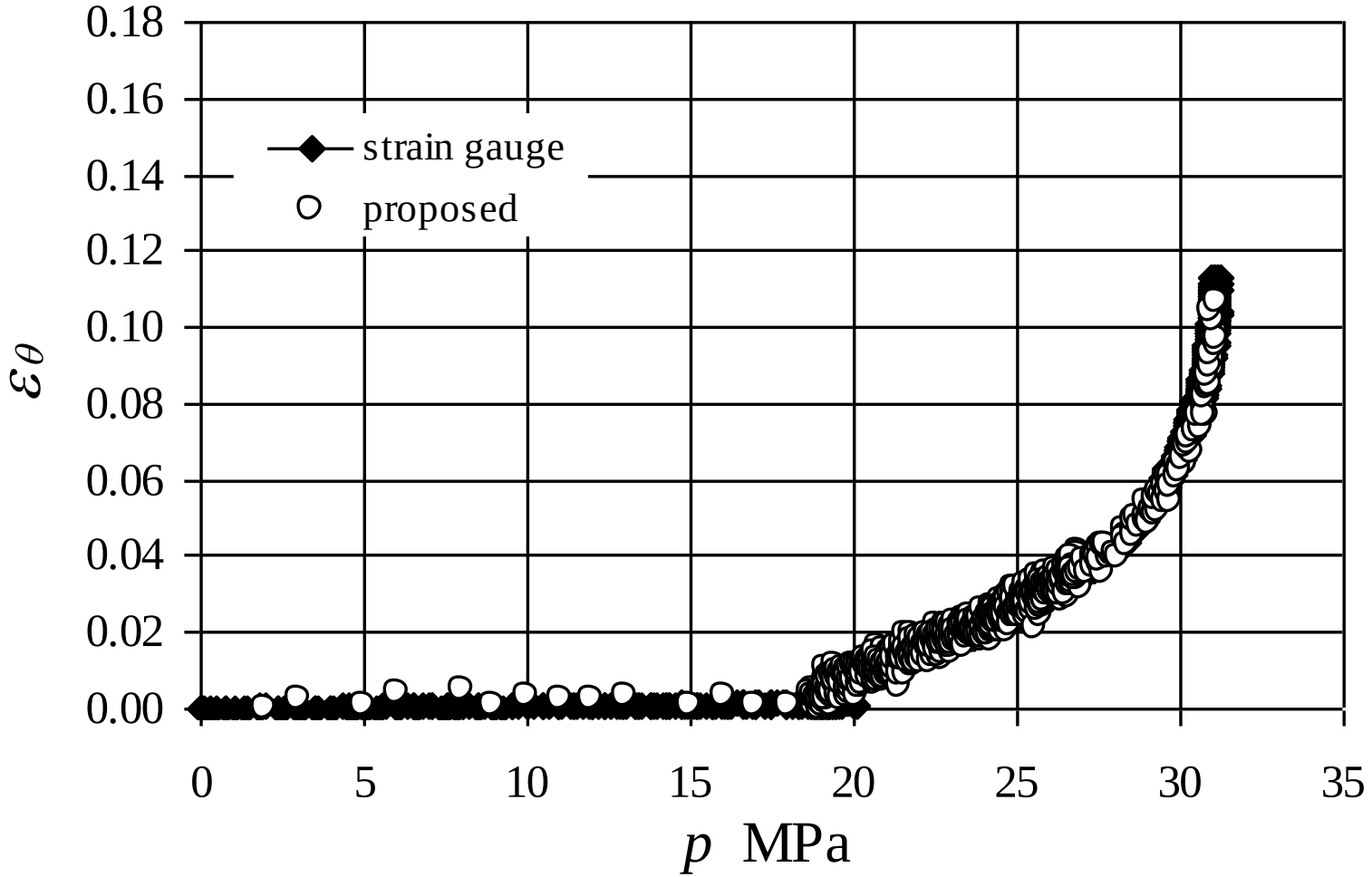

Fig. 10 Internal pressure-circumferential strain curve (ϕ = 15 deg, z = 15 mm)

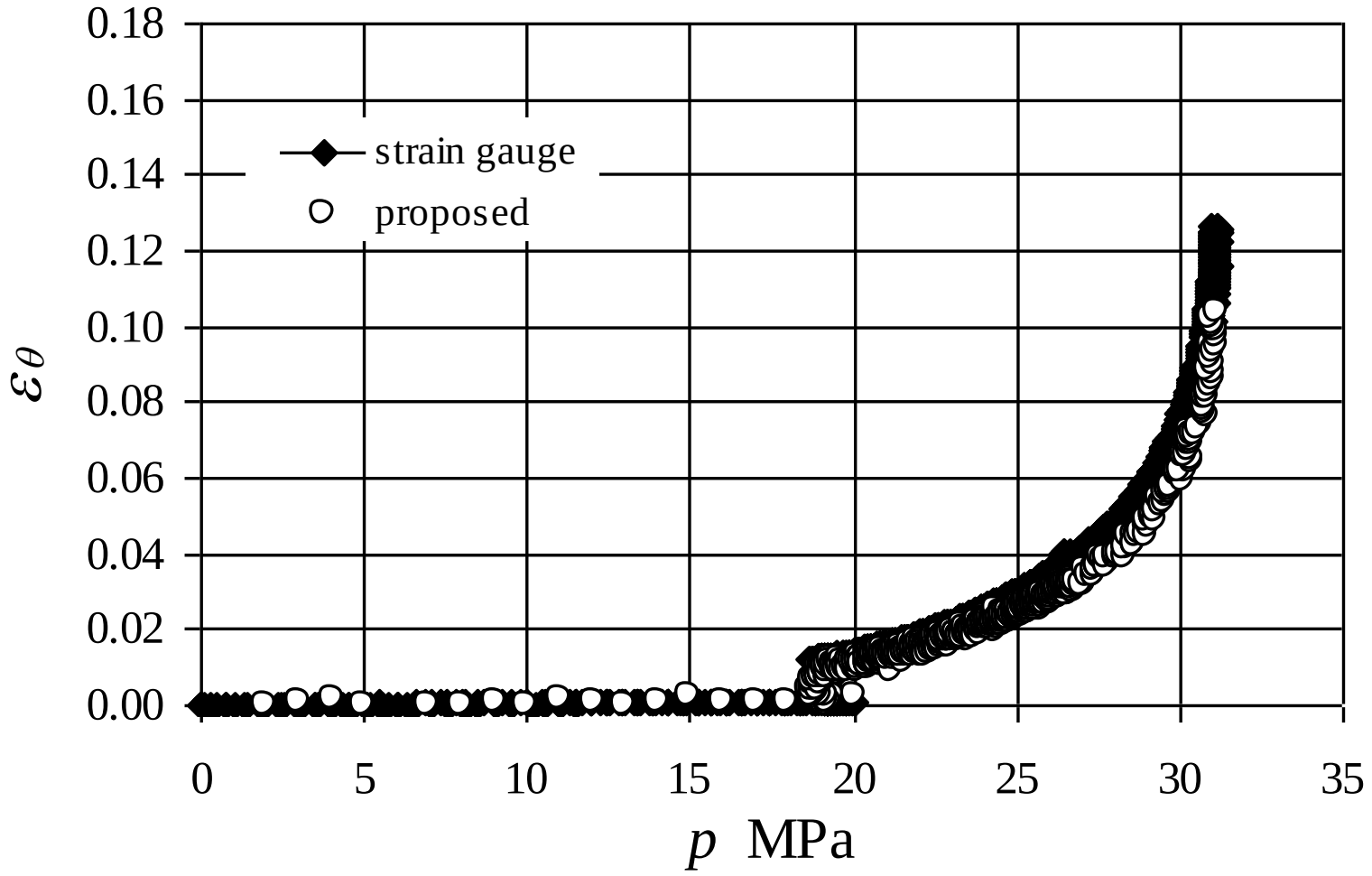

Fig. 11 Internal pressure-circumferential strain curve (ϕ = 175 deg, z = -15 mm)

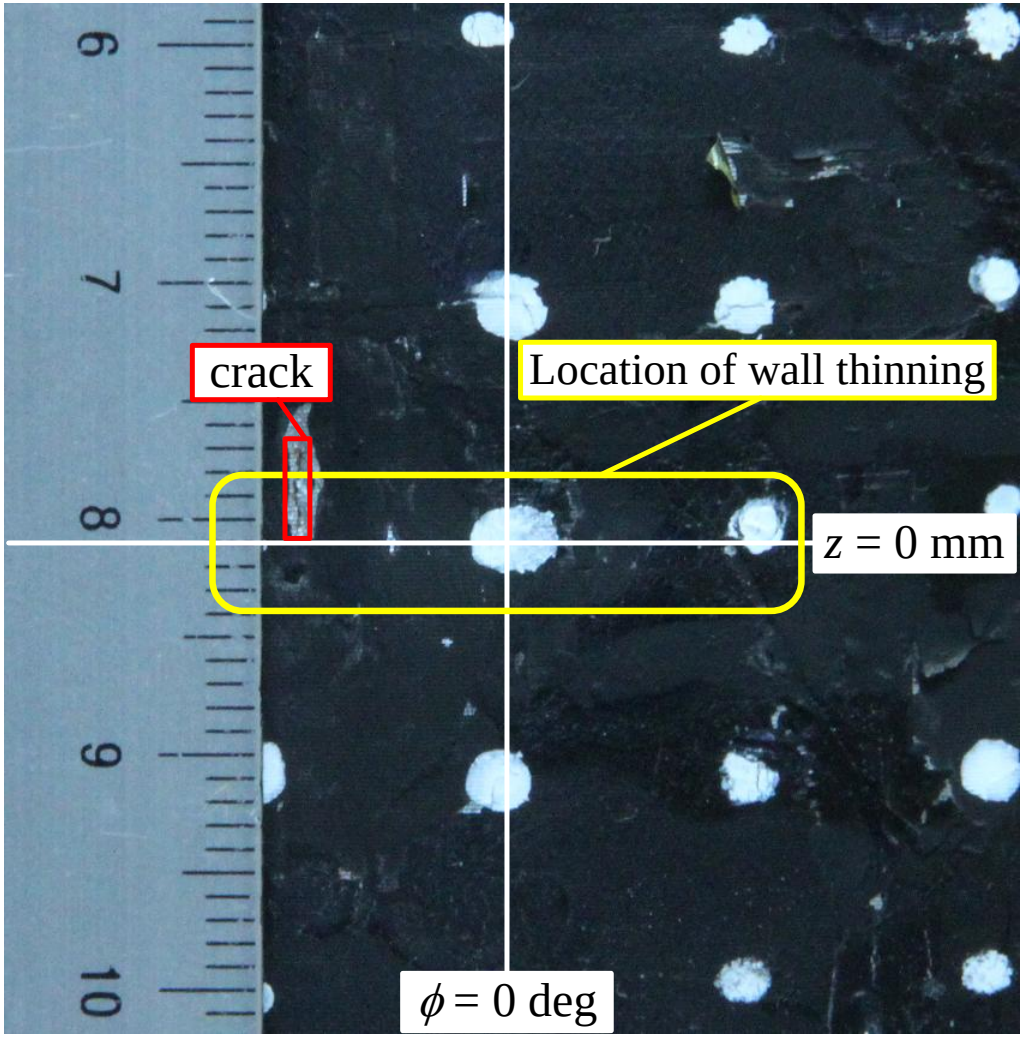

Fig. 12 Fracture appearance

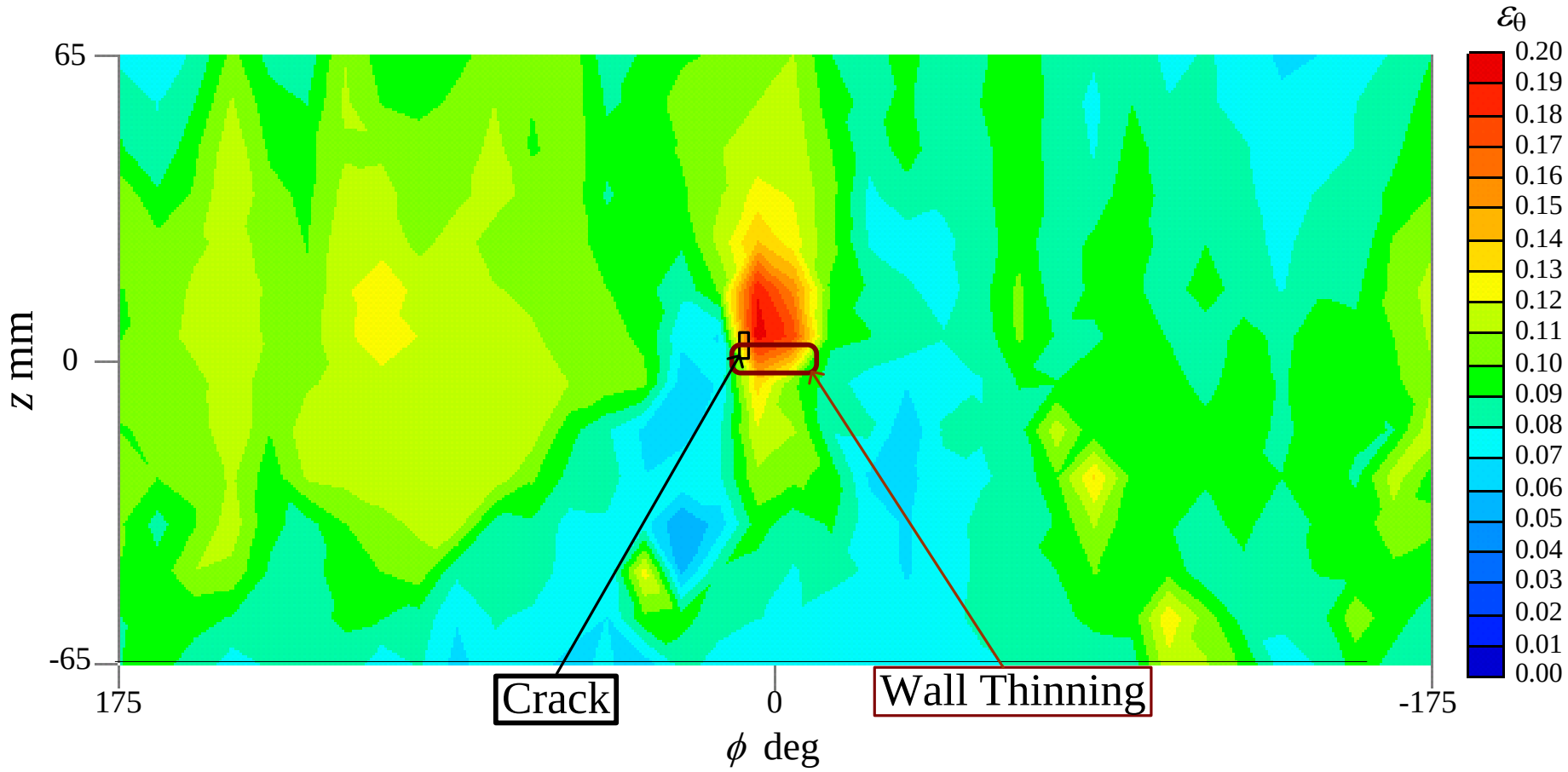

Fig. 13 Circumferential strain distribution ($p/p_f = 1$)

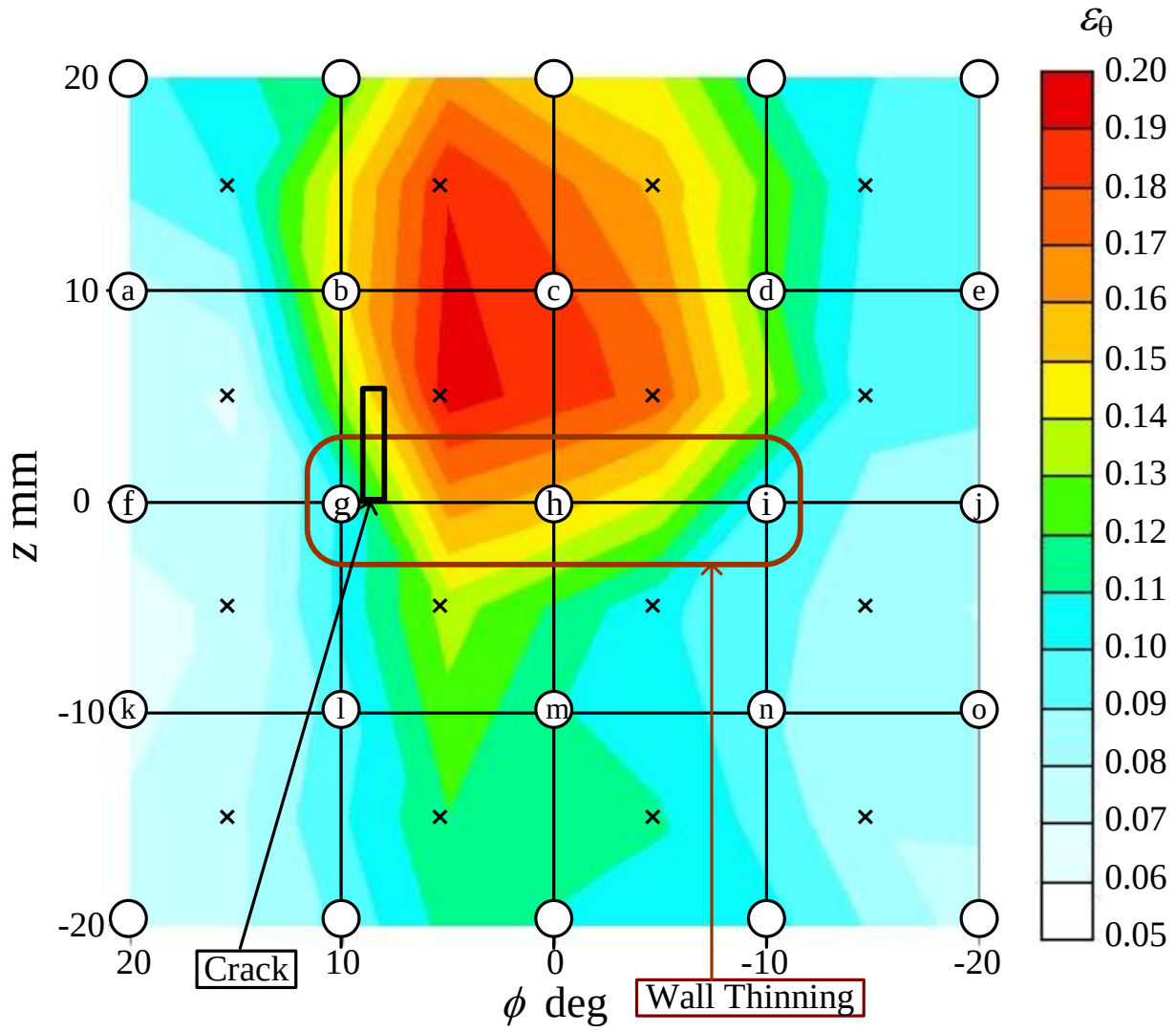

Fig. 14 Circumferential strain distribution
($p/p_f = 1$, z = -20～20 mm, ϕ = -20～20 deg)